ADVANCED MATERIALS TECHNOLOGIES
www.advmattechnol.de

Combining 3D Printing and Cryostructuring to Tackle Infection and Spine Fusion

Tiziana Fischetti, Gabriela Graziani, Daniele Ghezzi, Friederike Kaiser, Stefanie Hoelscher-Doht, Martina Cappelletti, Giovanni Barbanti-Bròdano, Jürgen Groll, Nicola Baldini, Uwe Gbureck, and Tomasz Jungst**

Low back pain is among the main issues in vertebral orthopaedics. Intervertebral disk degeneration can be severe, up to requiring the replacement of the damaged disk by substitutes to achieve spine fusion. Disk removal results in critical size defects, so fusion does not occur naturally, but synthetic bone grafts are needed. Since the surgical procedure is time-consuming, high infection rates occur. Hence, in spine fusion, bone regeneration enhancement and infection prevention are needed. Here, a new dual-component system is proposed, to tackle both issues at one time. To enable spine fusion, 3D extrusion-based printing is employed to develop coherent custom magnesium phosphate (CaMgP)-based cages. The 3D-printed scaffolds are hardened, and the structural properties are evaluated to be within the ranges of physiological bone. To prevent infection, an in-house ice-templating device is employed in combination with a 3D-printed ceramic scaffold, to develop tailored porous alginate structures loaded with vancomycin. Results show that CaMgP can be printed into complex geometries and that the geometry influences the pore orientation during ice-templating. These structures loaded with vancomycin have antibacterial properties against *Escherichia coli* (*E. coli*) and *Staphylococcus aureus* (*S. aureus*) strains.

1. Introduction

Spinal fusion surgery is among the most frequent orthopaedic procedures, accounting for over 400,000 cases per year in the U.S. only, with high societal and economic burden.[1–4] Spinal fusion procedures are often performed to address various disorders such as disk disease, disk herniation, segmental instability, trauma, and spinal deformities.[5] The most important aims in spinal fusion are to i) permit optimal fusion between adjacent vertebrae and ii) prevent infection. The gold standard for spinal fusion is the combination of polymeric (polyetheretherketone, PEEK) or metallic (titanium) cages with bone autografts (bone retrieved from the iliac crest), the latter having inherent osteogenic, osteoinductive, and osteoconductive properties that can enhance the healing process and the effectiveness of fusion. However, autografts are associated with donor site morbidity, limited availability, increased blood loss, and prolonged operative time.[6] Regarding alternative solutions to autografts, extensive research has been performed, allowing to develop several different synthetic bone grafts. Among these, the most promising materials include ceramics (mainly calcium phosphates or bioactive glass-based), eventually combined with polymers. 3D printing technology is often used as it allows to

T. Fischetti, G. Graziani, N. Baldini
Biomedical Science and Technologies and Nanobiotechnology Laboratory
IRCCS Istituto Ortopedico Rizzoli
via di Barbiano 1/10, Bologna 40136, Italy
D. Ghezzi, M. Cappelletti
Department of Pharmacy and Biotechnology
University of Bologna
Via Irnerio 42, Bologna 40126, Italy

The ORCID identification number(s) for the author(s) of this article can be found under https://doi.org/10.1002/admt.202301301

DOI: 10.1002/admt.202301301

F. Kaiser, J. Groll, U. Gbureck, T. Jungst
Department for Functional Materials in Medicine and Dentistry
Institute of Functional Materials and Biofabrication
University of Würzburg
Pleicherwall 2, D-97070 Würzburg, Germany
E-mail: uwe.gbureck@uni-wuerzburg.de;
tomasz.juengst@fmz.uni-wuerzburg.de
S. Hoelscher-Doht
Department of Trauma, Hand, Plastic and Reconstructive Surgery
University Hospital of Würzburg
Oberdürrbacherstraße 6, 97080 Würzburg, Germany
G. Barbanti-Bròdano
Department of Spine Surgery
IRCCS Istituto Ortopedico Rizzoli
via di Barbiano 1/10, Bologna 40136, Italy
N. Baldini
Department of Biomedical and Neuromotor Sciences
Alma Mater Studiorum-University of Bologna
via Massarenti 9, Bologna 40138, Italy

design customized geometries and shapes of the construct, with the desired properties in terms of material, biomechanical, and biological features.[7–9] Previous studies developed 3D printed scaffolds for cervical fusion cages by using silk fibroin and hydroxyapatite (HA),[10] polycaprolactone (PCL) alone[11] or combined with tricalcium phosphate (TCP),[5] polylactide-co-glycolide (PLGA) copolymer and HA.[6,12] They obtained mechanical properties comparable to those of the native bone. The first scaffolds for fusion were generally constituted by HA, but nowadays research is shifting toward faster degrading compounds, such as brushite and TCP. Although not widely investigated for 3D printing, magnesium phosphates cements are emerging as a promising alternative to calcium phosphates. Indeed, magnesium exerts a positive biological role and magnesium phosphates can be chemically converted into struvite that shows faster degradation/bone regeneration profiles. Literature data on rabbits and sheep models show that struvite dissolution leads to in vivo tissue ingrowth within 4 months and to complete bone regeneration in 10 months, with no signs of inflammation or rejection.[13–17] Regarding the approaches for 3D printing of cements, the existing ones focus on the use of 3D powder printing to combine cement powder and an aqueous binder solution. However, powder printing is limited to the use of monolithic materials. Recently, extrusion-based 3D printing has been proposed for calcium phosphates and derivates (e.g., magnesium phosphates).[1,13] Indeed, 3D extrusion-based printing enables the printing of polymer-ceramic composites simultaneously processed in one scaffold. The included polymeric phase can positively act as a viscosity modifier during the 3D printing process.[13]

Regarding infection, the occurrence rate in spine surgery is high and ranges from 0.2% to 16.7%,[3] depending on the diagnosis and on specific factors contributing to infection risk increase, such as comorbidities, duration of the surgical procedures, and type of surgical access. In the case of infection, implant removal and revision surgeries are frequently needed. Moreover, infection and failure rates further increase in revision surgeries.[8] Due to these obstacles, implant-related infection is an unresolved and critical problem, and its prevention and treatment are object of extensive investigation. To prevent infection, local delivery of antibiotics in the implantation site is desired to aid systemic therapy. To date, this is obtained by submerging the prosthesis in antibiotic solutions, prior to implantation. However, this leads to i) a scarce control over drug release profile and ii) a scarce duration of the antibacterial effect. For these reasons, loading the drugs in biomaterial carriers is a promising strategy to obtain controlled release. As such, hydrogels have been considered for drug loading and release applications.[8,18–21] Together with the composition of the material, also the morphology can be exploited to tune loading and release, and different strategies have been pursued to obtain porous materials, adequate for loading. In particular, the development of porous hydrogels by traditional or innovative ice-templating techniques is promising,[22–26] as unique architectures can be introduced. Among the novel ice-templating techniques, cryostructuring enables a high level of control over the pore structures. The working principle is based on the application of a controlled external temperature gradient to unidirectionally freeze a polymeric solution. After freezing, the grown ice crystals are removed via freeze-drying, and the final pores morphology is the negative template of the original ice crystals.[27–29] Cryostructuring technique has several advantages, including versatility, ease of use, and process scalability.[29] Moreover, it allows to obtain highly anisotropic porous structures and to tune the pore orientation and size.[28] This feature could be useful in our studies and in drug-loading applications, where the control of drug adsorption and release rate is desired.

In this work, we introduce different elements of novelty, such as i) the use of magnesium phosphate (CaMgP) scaffolds for the 3D printing of complex customized geometries, ii) the combination of 3D printing and ice-templating technologies to achieve both osseointegration and infection prevention, and iii) the investigation of cryostructuring technique [28,30] for antimicrobial or drug loading applications.

More in detail, we propose the use of CaMgP together with a polymeric phase to develop a paste for 3D extrusion-based printing. Custom-shaped cages for lumbar spinal fusion were designed, and the 3D printing process and parameters were optimized. The obtained 3D printed scaffolds were characterized by means of printing accuracy, phase composition after chemical reaction, stability, and mechanical properties, aiming to evaluate the suitability for the application.

To address infection prevention, the 3D printed scaffolds were combined with freeze-structured porous alginate loaded with an antibiotic drug. The use of alginate as drug delivery system in bone defects in the presence of infection has been previously reported.[31–33] In this study, first the cryostructuring process was investigated alone by testing different temperature gradients and alginate concentrations to analyse the pores formation process, in terms of pores morphology, orientation, and size. Then, cryostructuring and 3D printing were combined to evaluate the effect of the 3D printed structure on cryostructured pores. Indeed, 3D printing could positively influence the crystal growth, and hence the pore size and distribution in the final scaffold. Consequently, this allows to tune the mechanical and biological properties of the system. Furthermore, combining these techniques enables creating a tight connection between the 3D-printed CaMgP scaffold and the cryostructured alginate, thus conferring mechanical integrity to the system. The interest in combining advanced manufacturing technologies (i.e., melt electrowriting, 3D-printing, volumetric printing) to develop functional tissues is growing,[34–36] however, to date, a combination of extrusion-based 3D printing and cryostructuring has not been investigated. To demonstrate the suitability of cryostructuring for drug delivery applications, alginate was loaded by vancomycin drug. This was performed i) by preloading the vancomycin drug before cryostructuring and ii) by post-loading the vancomycin drug via soaking the scaffold in the antibiotic solution after cryostructuring. The post-loading condition mimics the standard surgical procedure. The pre- and post-loaded cryostructured scaffolds were used for the evaluation of their antibacterial activity against two of the main pathogenic bacterial strains responsible for orthopaedic infections, i.e., strains of *Escherichia coli* (*E. coli*, gram-negative) and *Staphylococcus aureus* (*S. aureus*, gram-positive). The composite structures constitute a promising solution to enhance bone tissue formation and face the occurrence of infection during the early stages of implantation.

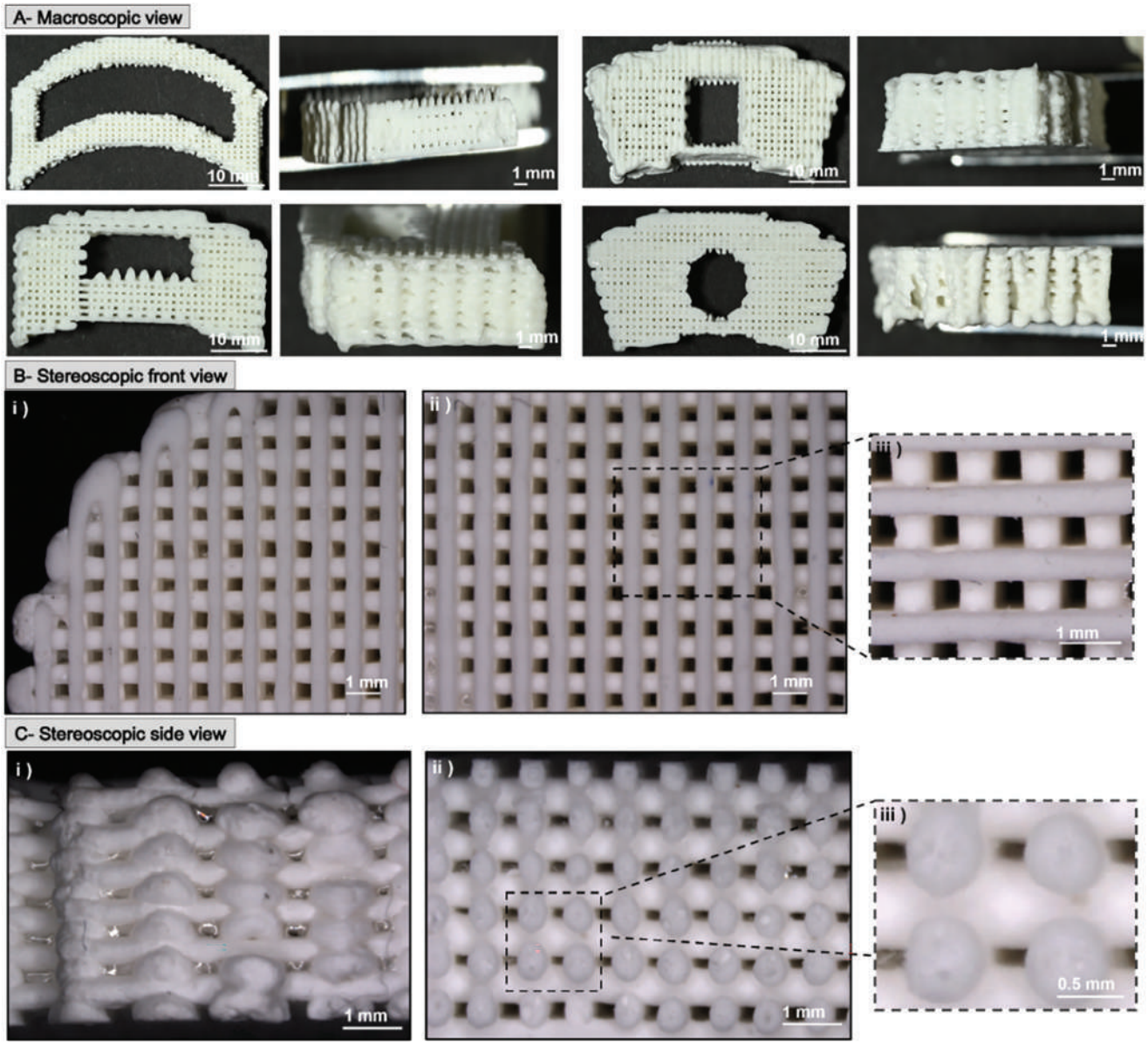

Figure 1. A) Macroscopic and B,C) stereoscopic views of the 3D printed scaffolds. A) Front view and side view for each designed geometry and 3D printed scaffold, B) Top view of the 3D printed scaffold in the i) border, ii) center, and iii) zoom of the 0–90° square pattern. Scale bar: 1 mm. C) Side view of the 3D printed scaffold, and in detail i) height , ii) fracture surface, and iii) zoom of the pores.

2. Results and Discussion

2.1. Development and Characterization of the 3D Printed Structure

2.1.1. 3D Printing Optimization Process and Print Fidelity Evaluation

Mixing CaMgP components, water (powder-to-liquid ratio, PLR = 1.35 g mL^{-1}), and hydroxypropylmethylcellulose (HPMC) manually and by a planetary mixer allowed to obtain a bubble-free and uniform slurry. Moreover, aging over 24 h increased the viscosity and improved extrudability of the paste, which was necessary to successfully print the paste by extrusion-based 3D printing. The printing pressure was in the 1.1–1.3 bar range, with this value varying for increasing paste viscosity over printing time. The set pressure values and the 22 G nozzle ensured the continuous extrusion of the paste, with limited clogging. Hence, CaMgP-based 3D printed structures with different complexity, shape, and dimensions were obtained (**Figure** 1A; Figure S1, Supporting Information). The selection of different shape designs and dimensions (i.e., inner geometry, height) was done to evaluate the 3D printing process versatility. Moreover, the inner shape of the 3D printed structures was varied to evaluate the effect of the 3D printing geometry on the morphology of the cryostructured scaffolds, when combining the two techniques.

Here, the 3D printing of complex structures with different geometries compatible to custom shaped cages for spinal fusion surgery was successfully obtained, with dimensions (40×20 mm length x width, up to 7 mm in height) suitable to be combined with cages (existing options have 34 × 24 mm, 38 × 28 mm, 42 × 30 mm as width x length, and 6-8-10-12 mm in height)[37] and acceptable accuracy value (>75%).[13] The pores within the 3D printed structures were highly interconnected, as shown in the front (Figure 1B) and side views (Figure 1C) of the scaffolds. Additionally, the pores exhibited a square geometry (Figure 1B-i,ii), which corresponds to the designed 0–90° pattern (Figure 1B-iii). Moreover, the pore width has been measured (Figure 1B-i) and an average dimension of 500 ± 5.8 µm (nominal width being 1 mm, i.e., fiber spacing), i.e., within the optimal physiological range to permit bone ingrowth (100–500 µm),[9,38,39] was obtained.

The average fiber dimension is 514.4 ± 3.2 µm. This value is 25% higher than the nozzle dimension (nominal value 410 µm) resulting in an accuracy equal to 75%. From the lateral view images, the different layers can be clearly seen and defined (Figure 1C-i). In Figure 1C-ii the fracture surface of the construct is displayed, and it can be observed that the morphology is regular (zoom in Figure 1C-iii). Thus, comparing these results to accuracy evaluations (ranging 80–85%) in the literature on 3D printed ceramics,[40–43] it can be stated that it was possible to obtain 3D printed CaMgP based-scaffolds with high reproducibility and printing fidelity, also when increasing the geometrical complexity and scaffold dimensions. Moreover, the obtained structures show that the geometry and design can be tailored to be combined with cryostructuring, and the pores are in a size range that favors bone formation. Thus, the obtained scaffolds are promising for clinical translation and spinal fusion applications.

2.1.2. Phase Determination by X-Ray Diffraction and Rietveld Method

The different chemical compositions, obtained by finely grinding the 3D printed scaffolds and determined by X-ray powder diffractometry, are shown in Figure S2 (Supporting Information). The reaction between the 3D printed magnesium phosphate scaffolds (in which main phases are farringtonite $(Mg_3(PO_4))_2$ and stanfieldite $(Ca_4Mg_5(PO_4)_6)$, added by periclase (MgO)) and diammonium hydrogen phosphate ($(NH_4)_2HPO_4$, DAHP) lead to the formation of magnesium ammonium phosphate hexahydrate (struvite), and minor magnesium-based (i.e., newberyite) and calcium-based (i.e., brushite) by-products.

Among these reaction products, struvite permits hardening of the samples.[44] For the mentioned phases, the quantitative content before/after conversion treatment was determined and reported in Table S1 (Supporting Information). Both farringtonite and stanfieldite contents were reduced in the converted conditions (vs CaMgP+MgO+HPMC condition). Although farringtonite and stanfieldite phases are biocompatible, they are characterized by lower solubility compared to struvite, so their presence is undesired.[17] Regarding struvite, similar contents were obtained among the different hardening times (p-value > 0.05). Thus, increasing the hardening time in the DAHP solution did not enhance further conversion into struvite. The sintered scaffolds demonstrated a slightly reduced conversion to struvite, although not statistically significant (p-value > 0.05). Thus, the sintering process partially inhibited the reaction between MgO and DAHP. Based on these results (struvite conversion efficacy and time), content of undesired (i.e., farringtonite/stanfieldite) and impure (i.e., periclase) phases, curing by immersion in DAHP solution for 24 h was selected, while all other conditions (i.e., 36H DAHP, 48H DAHP, SINT+24H DAHP) were discarded.

2.1.3. Mechanical Characterization

The mechanical properties of the 3D printed structures were evaluated in static and dynamic mode. Results of static mechanical tests (day 0) are shown in **Figure 2**A. When 3D printed samples with different fiber spacing were compared, a decrease in compressive strength was noticed for increasing fiber spacing. This is caused by the increase in porosity with increasing fiber spacing. The inverse relationship between porosity and compressive strength is a design tool that allows to fine-tune mechanical properties in 3D printing technology.[45–48] In this study, the measured compressive strengths were 9.3 ± 1.9 MPa for the 1 mm fiber spacing, 5.7 ± 1.1 MPa for the 1.5 mm fiber spacing, and 4.4 ± 0.5 MPa for the 2 mm fiber spacing, respectively. The difference in compressive strength was statistically significant for the groups 1 mm versus 1.5 mm and for the 1 mm versus 2 mm fiber spacing. In summary, the obtained compressive strength values were in the range of 4–10 MPa for the 3D printed structures with different fiber spacing (i.e., 1, 1.5, 2 mm). These values are very close to the ones (4.3–11 MPa) reported for powder 3D printed constructs with the same material composition ($Ca_{0.75}Mg_{2.25}(PO_4)_2$) and post-hardened by sintering and DAHP immersion.[17] Moreover, the compressive strength values found in the present study are in the range of native cancellous bone (0.5–15 MPa),[49,50] which means the scaffolds are suitable to be combined with spinal fusion cages. The compressive strength values for the 1 mm fibers spaced samples were evaluated over 28 days (Figure 2B) storage in phosphate buffer saline (PBS), and no statistically significant differences for the whole immersion period (p-value > 0.05) were observed, indicating that mechanical properties of the scaffolds are stable for over 28 days. The high standard deviations can be related to the intrinsic differences present within the different 3D printed samples (e.g., presence/absence of irregularities within the samples, small differences of the contact surface orientation/area during mechanical testing).

During dynamic mechanical loading, the scaffold stability highly depended on the fiber spacing. Some of the samples with 1.5 and 2 mm fiber spacing were not able to reach the necessary axial load of 300 N after the settling cycles, resulting in immediate failure. Additionally, the ones reaching the 300 N survived <100 cycles on average (Table S2, Supporting Information), breaking relatively early within the dynamic testing period. Thus, the higher porosity obtained both for 1.5 and 2 mm fiber spacing negatively affected their resistance to cyclic loading.

For the 3D printed samples with 1 mm fiber spacing, 4 of 5 samples were capable of sustaining over 5000 cycles at the fixed load (300 N, 0.9% deformation) without experiencing failure. On average, they survived 4943 ± 141 cycles.

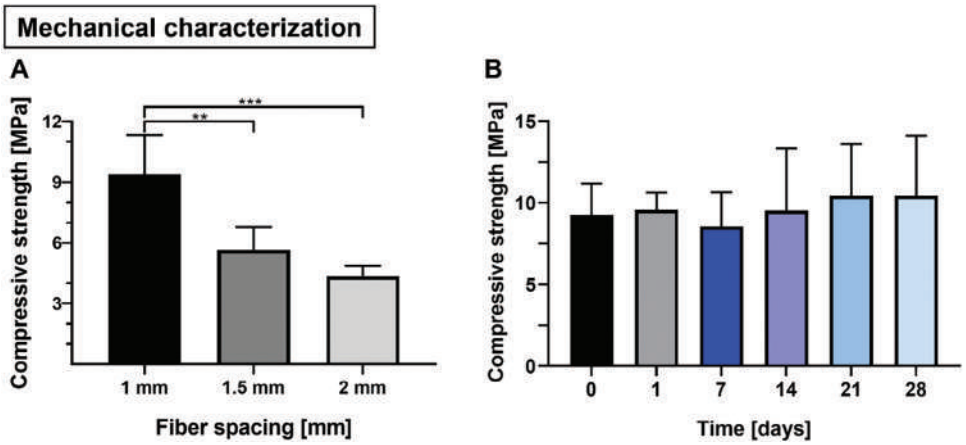

Figure 2. A) Compressive strength of hardened 3D printed magnesium phosphate scaffolds for different fiber spacing (1, 1.5, 2 mm) and B) for 1 mm fiber spacing over time (up to 28 days storage in phosphate buffer saline). Two-way ANOVA with post-hoc Tukey test between experimental groups (data presented as mean ± SD, $n = 5$, $^{**}p$-value ≤ 0.01, $^{***}p$-value ≤ 0.001).

The maximum load, also defined as failure load, was ≈1100 N, and the compressive strength was 12.6 ± 3 MPa. This value is comparable to the one found in static mode (i.e., 9.3 ± 1.9 MPa), and comprised within the reported compressive strength range of printed ceramic scaffolds (0.1–21.2 MPa)[13,42,43] and of cancellous bone.[43] Hence, the 1 mm fiber spacing scaffolds were able to maintain the compressive strength values even after being subjected to 5000 cycles and thus proved to be highly durabley. Moreover, it has to be highlighted that the developed scaffolds are not intended to be implanted alone but combined with a commercially available cage. This means that the loads will not act directly on the scaffolds, but the obtained mechanical properties of the 3D printed scaffolds could be beneficial to further promote the bone regeneration process. Because the 1 mm fiber spacing samples achieved the highest compressive strength and cyclic loading survival, they were chosen for all further experiments.

2.1.4. Ion Release Study and Stability Test

The release of Mg^{2+} and Ca^{2+} ions from CaMgP bulks and 3D printed samples was investigated over 28 days (**Figure 3**A,B) storage in PBS. The Mg ion release (Figure 3A) of bulks and 3D printed samples was similar, characterized by a constant increase in Mg ion release over time.

The Ca ion release profile (Figure 3B) was also similar between bulks and 3D printed samples, with a trend of increasing release over time. As previously reported for the mechanical properties, the standard deviations in the 3D printed samples are higher than in the bulk samples. Thus, although the magnesium ion release is slightly lower in the 3D printed samples (where a higher release could be expected due to a higher surface porosity) versus the bulk samples, the difference is not statistically significant.

Comparing Mg and Ca ions release, it can be assessed that the release was increasing over time and more pronounced after 7 days for both ion types, thus being promising to promote fast bone tissue repair.[14,17,51–53] In addition, the value of Ca ions release is about ten times lower than the Mg ions release, due to the lower content of Ca in the CaMgP powder formulation (1:3 molar ratio of calcium: magnesium) and in accordance to previous studies on comparable cement compositions.[14,54]

In Figure 3C, stability test is reported for samples immersed in PBS at different timepoints. An initial weight loss (−10%, ≈ 90 mg) was recorded on the first day, followed by 0.7% (≈6 mg) weight decrease after day 1 and up to 28 days. This dissolution behavior is mainly due to the partial dissolution of the polymeric viscosity modifier (HMPC), but it could be also related to the CaMgP degradation, although to a lower extent. Thus, it can be stated that the weight was almost stable and decreased by 11% over 28 days. These results are expected under in vitro conditions, as the struvite solubility in water at 25 °C is 8–119 mg L^{-1},[55] leading to a dissolution of 0.02–0.36 mg of the 3D printed samples once immersed in PBS, and to an estimated total struvite loss of 0.3–5 mg over 28 days (medium refresh every 2 days). Considering the higher temperature during incubation (37 °C), this matches the observed 6 mg weight loss caused by CaMgP dissolution. The slow in vitro degradation rate might be caused by a rapid saturation of the PBS solution with respect to Mg^{2+} and HPO_4^{2-} ions (compared to the in vivo condition, as reported in the Literature for similar materials).[17,51] A similar slow degradation of struvite cement bulk samples with a PLR of 1 g/mL in PBS has been previously observed, and a 1% weight loss was obtained after 18 days in PBS.[56] However, under in vivo conditions the biological fluids contribute to an increase in the struvite degradation rate, thus showing a high dissolution behavior.[17] Indeed, as previously reported, CaMgP paste underwent a complete degradation and regeneration of bone tissue over 6 months in vivo, with the largest bone growth between months 1 and 3.[17] This suggests that the CaMgP paste proposed here should degrade within a similar period rate in vivo. Regarding bone fusion, it has to be considered that the bone fusion period for adjacent vertebrae takes from 3 up to 6 months, with this time getting longer in patients affected by disorders or chronic diseases, as obesity, osteoporosis, or diabetes.[3] According to the previously obtained results on CaMgP paste in vivo dissolution and bone fusion period, the CaMgP-based 3D printed structures proposed here are promising for spinal fusion surgery application.

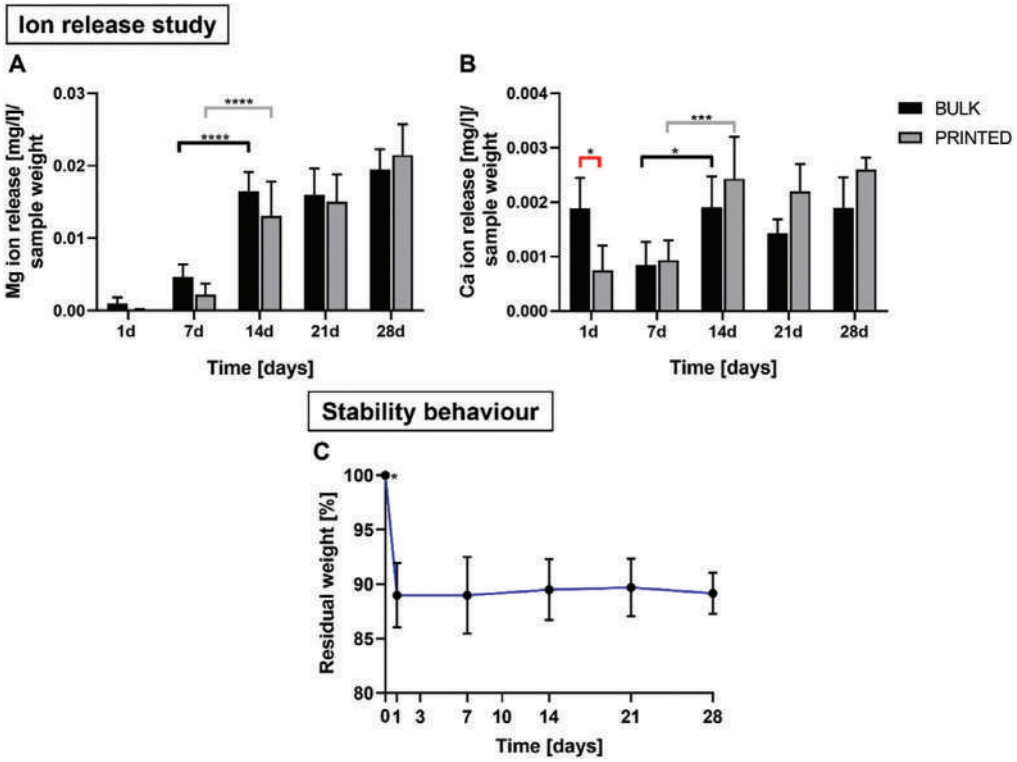

Figure 3. A) Cumulative ion release determined for Mg^{2+} ions, and B) Ca^{2+} ions normalized by bulk and 3D printed samples weight, respectively. C) Stability behavior in PBS solution, at 37 °C for the 1 mm fiber spacing 3D scaffolds. Two-way ANOVA with post-hoc Tukey test between experimental groups (data presented as mean ± SD, $n = 5$, $^{*}p$-value ≤ 0.05, $^{***}p$-value ≤ 0.001, $^{****}p$-value < 0.0001).

The 3D printed 1 mm fiber spacing CaMgP scaffolds hardened in DAHP for 24 h showed a high struvite content, stable mechanical properties (compressive strength ≈9 MPa) over 28 days and after 5000 cycles and were thus considered eligible to be further combined with cryostructuring.

2.2. Development of Cryostructured Scaffolds

2.2.1. Cryostructuring Process Evaluation and Combination with 3D Printing

Regarding cryostructuring of alginate alone, it has been previously shown that material concentration, molecular weight (MW), and consequently, viscosity, influence the process.[27] The most important parameters to control pore properties are temperature gradient, cooling rate, and the temperature set in the systems.[27] According to this, two different alginate concentrations (i.e., 1, 2% w/v) and different temperature gradients (2, 3, 4 K mm^{-1}) were tested to evaluate how the viscosity of the polymer solution affects the pore growth and orientation. In 1% w/v alginate, the pores were not aligned and did not follow a specific orientation, independent of the temperature gradient. At 2% w/v alginate, pores appeared more stable and regular, with a more homogeneous orientation (Figure S3, Supporting Information).

For this reason, 2% w/v alginate was used to analyse the pore properties (i.e., orientation, dimension) based on changing temperature gradients. At 2 K mm^{-1} pores orientation and dimensions were not homogenous (Ø = 229.7 ± 69.5 µm) resulting in high standard deviations, with some areas in which the pores change orientation. The same effect, although less pronounced, was obtained with the 3 K mm^{-1} temperature gradient (Ø = 116.6 ± 33.5 µm). By increasing the gradient to 4 K mm^{-1}, the pores showed homogeneous orientation and size, with more uniform dimensions resulting in lower standard deviation (Ø = 66.3 ± 14.7 µm). Hence, pore size decreased from 2 to 4 K mm^{-1}, according to previous results.[27] Due to the better results obtained with the 4 K mm^{-1} temperature gradient, it was selected for combination with 3D printing.

To combine the two technologies, the 3D printed construct was inserted inside the cryostructuring device, and the 2% w/v alginate solution was injected and frozen (4 K mm^{-1}) within the printed construct. After the lyophilization process, the 3D printed construct and the injected polymer were still anchored, and no detachment was observed between the two materials (Figure S4, Supporting Information). Thus, neither the freezing temperature nor the lyophilization negatively affect the 3D construct, and the two technologies can be combined to obtain a complex composite structure, with no negative shrinking effect. A process scheme showing the combination of 3D printing and cryostructuring is depicted in **Figure 4**. Regarding biological behavior, the CaMgP paste hardened by 3.5 M DAHP and the alginate used in this study have been separately evaluated in previous studies,[17,57] with positive results on cell viability. Thus, it is reasonable to assert that the dual component system here proposed is cytocompatible and promising for spine fusion and bone applications. An

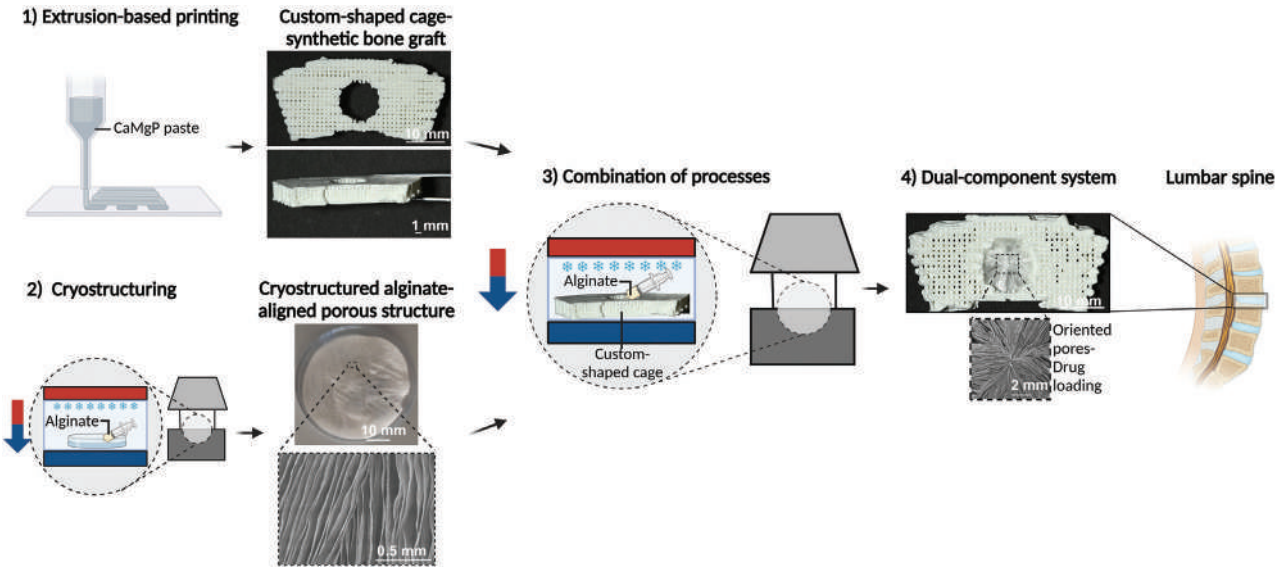

Figure 4. Schematic process to develop the dual component system by 3D extrusion-based printing and cryostructuring technologies, intended for lumbar spine fusion treatment. Created with BioRender.com.

in vivo validation of the system is envisioned in future to proceed toward clinical applicability.

Interestingly, in the 3D printed construct, the cryostructured alginate showed highly aligned pores and homogenous pore dimension. Moreover, the pore geometry depends on the 3D printed inner shape (Figure S4A–D, Supporting Information; Figure 5B, top and bottom), while in alginate alone only some aligned domains can be recognized (**Figure** 5A, top and bottom). Thus, the presence of 3D printed constructs led to an increase in pores alignment and a geometry-dependent effect, with higher process control and more reproducible results.

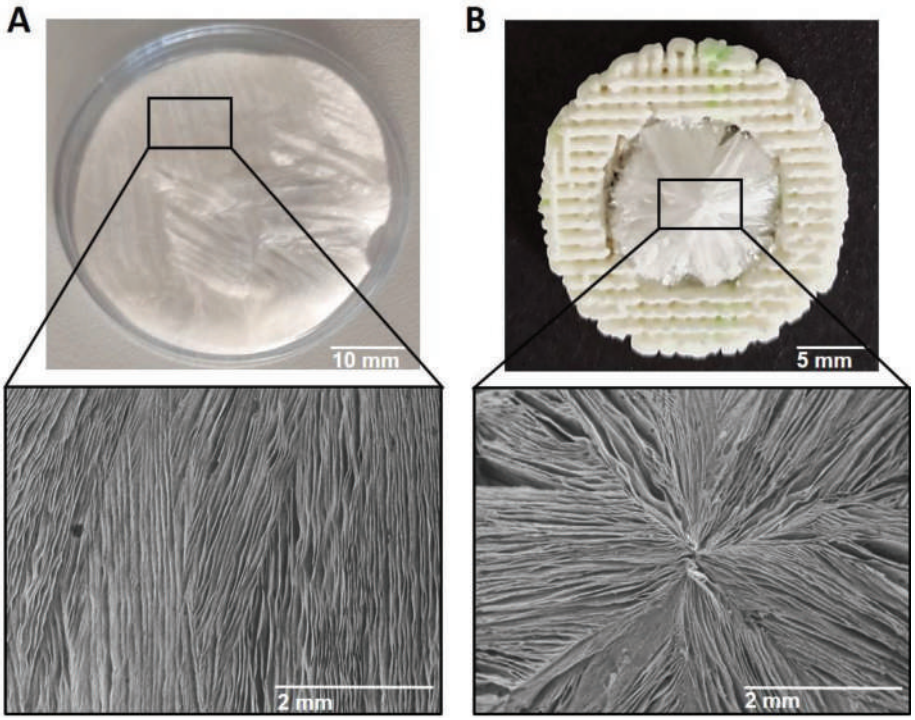

Figure 5. Cryostructured alginate by pouring the alginate solution in the Petri dish cover ((A), on the top) and SEM image of the selected area ((A), on the bottom). Cryostructured alginate by pouring alginate solution within the 3D printed construct ((B), on the top) and SEM image of the selected area ((B), on the bottom). SEM images Magnification: 30X.

Regarding the freezing behavior occurring in alginate alone and within the 3D printed structure, it can be observed that in the latter the freezing process started from the point more prone to temperature changes (i.e., the farthest from the 3D printed part), as less resistant to freezing, and continued toward to the outer part (i.e., the area closest to the 3D printed part). This can be attributed to the insulating nature of the 3D printed ceramic material. Regarding the geometrical influence of 3D printed structures on forming pores, it can be observed that for the geometries in Figure S4A,B (Supporting Information) the freezing process started with a curved line (appearing as a close and non-porous line), while for the geometries in Figure S4C,D (Supporting Information) it started from a central single point, indicating an impact of the symmetry of the hole on the cryostructuring process.

Since the 3D printed CaMgP cages combined with cryostructuring were able to influence the cryostructured pore formation, this can be considered for applications in which guided oriented pores and dimensions are desired. For example, the here proposed dual component system could serve as a platform to guide cell alignment. Previous studies from the patent's group already observed a positive effect on cell behavior (in terms of faster colonization and migration) played by anisotropic cryostructured scaffolds,[28,58] compared to other studies with similar pores size (80 µm)[59] or random pores orientation.[28] Thus, the enhanced effect might be related to the anisotropic orientation. In the dual component system proposed in this study, the cell guidance phenomenon could be even enhanced and tailored, as the 3D printed CaMgP cage surrounding the cryostructured alginate is also influencing the pores orientation behavior. Furthermore, sacrificial ceramic cages can be used to guide pore formation in cryostructured samples, even when they are to be used alone.

To further investigate the effect of different temperature gradients (2 and 4 K mm^{-1}) on pore formation, we selected the circular and rectangular inner geometries (**Figure 6**). Because the outer part of the scaffold did not affect the behavior of cryostructuring, results were collected on circular and smaller samples CaMgP cages , while the inner holes for the selected geometries were kept unvaried.

The difference between 2 and 4 K mm^{-1} temperature gradients is not pronounced within rectangular and circular geometries, thus hampering a real comparison in the pore behavior. However, it can be observed that in the circular geometry at 2 K mm^{-1} (Figure 6, on the top) the pores are characterized by slightly different shapes and sizes between them, while at 4 K mm^{-1} the pores are more reproducible and share similar shape and size.

For the rectangular geometry (Figure 6, on the bottom), the obtained pores do not show a clear trend at 2 and 4 K mm^{-1}, but pore domains with similar size and shape can be distinguished throughout the sample. In general, comparing the different geometries and temperature gradients, it can be concluded that the circular geometry at 4 K mm^{-1} shows pores with more homogeneous size and shape. However, the difference in pores size and shape observed for the other conditions should not be seen as a disadvantage. Indeed, this means that the geometry of the 3D printed construct and the different temperature gradients could affect the pore characteristics, and thus several patterns can be tailored.

2.2.2. Antibacterial Efficacy of Drug-Loaded Cryostructured Scaffolds

Antibacterial test activity was evaluated on bulk and cryostructured samples (4 K mm^{-1}, circular geometry) that were pre- and post-loaded (i.e., pre- and post- refer to before and after the cryostructuring process, respectively) with 6% w/v vancomycin drug, against the growth of 1 g negative and 1 g positive model bacterial strains (*E. coli* and *S. aureus*, respectively). This test was performed to detect the difference between the sample types (i.e., bulk and cryostructured samples) and drug-loading condition (i.e., drug loaded within the alginate solution in pre-loading condition, and after $CaCl_2$ crosslinking of cryostructured alginate in post-loading condition).

Figure 7 shows that vancomycin has a marked antibacterial activity for all tested conditions, i.e., bulk and cryostructured, pre-loaded and post-loaded samples.

Bulk samples pre-loaded with vancomycin drug induced an average of 4.6 log reduction (corresponding to 99.997% CFUs reduction) of *E. coli* growth compared to non-loaded bulks. These pre-loaded bulk samples showed the maximum efficacy against *S. aureus* leading to complete cell death when added to the bacterial culture. When vancomycin post-loaded samples were tested, they showed the capacity to completely eradicate both bacterial cultures.

Cryostructured samples pre-loaded with vancomycin drug induced a 5.4 log reduction (corresponding to > 99.999% CFUs reduction) of *E. coli* growth compared to non-loaded cryostructured samples. Similarly, to bulk samples, total cell death was observed when *S. aureus* cells were cultivated with pre-loaded cryostructured samples and when both strains were cultivated with post-loaded cryostructured samples.

The different sensitivity observed between *E. coli* and *S. aureus* in the presence of the antibiotic can be associated with the higher toxicity of vancomycin exerted against gram-positive bacterial strains.[60,61] Vancomycin inhibits the biosynthesis of the D-Ala-D-Ala dipeptide composing the peptidoglycan that is the main constituent of the gram-positive cell wall.[62] Since the outer membrane of gram-negative strains acts as a barrier to avoid the entrance of vancomycin, high concentrations of this antibiotic are needed to observe an inhibitory effect.[63] In line with this, the higher antibacterial activity observed when *E. coli* was cultivated with pre-loaded cryostructured samples is probably because of their higher porosity compared to the pre-loaded bulk samples. On the other hand, *S. aureus* growth was inhibited by pre-loaded drug samples regardless of the sample type (i.e., bulks and cryostructured samples). In the presence of post-loaded drug samples, total cell death was observed for both strains, again regardless of the sample type.

The difference in growth inhibition obtained with the pre- and post-loaded samples can be related to the following factors: i) efficacy loss of the drug in the pre-loaded samples due to low cryostructuring temperature, ii) drug loss during lyophilization process (i.e., water removal), resulting in a residual lower drug concentration in the pre-loaded samples, iii) different drug adsorption mechanism in pre- and post-loaded samples, and specifically higher on the core and on the surface of the structures, respectively. Aside of these drawbacks, in this study it was possible to successfully pre- and post-load vancomycin drug within the pores (Ø = 65 µm) of cryostructured alginate. These pore

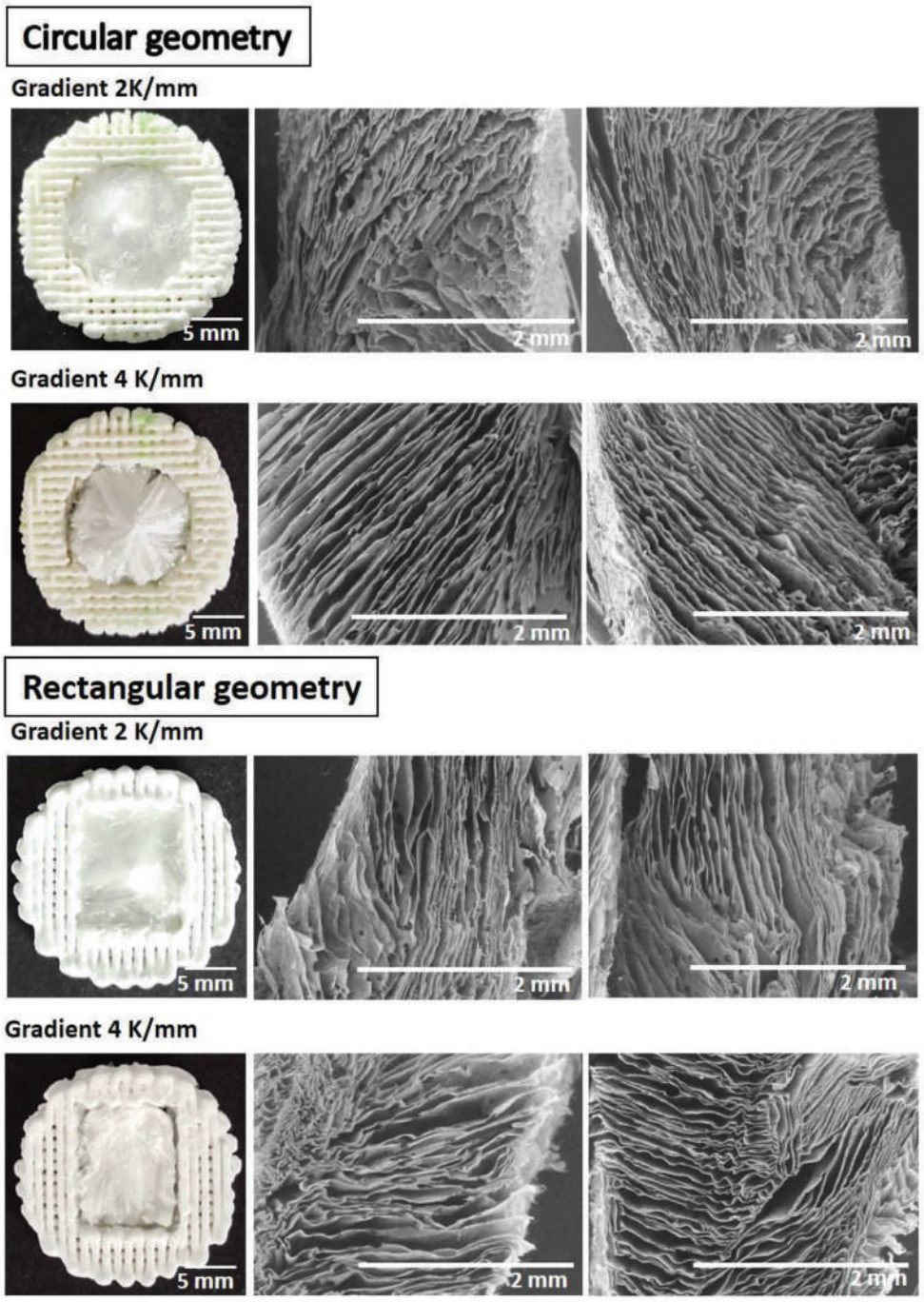

Figure 6. **(Circular geometry)** Macroscopic image of 3D printed sample with inner circular geometry for 2 K mm^{-1} gradient (left on the top), SEM cross-section images of samples (center and right, on the top), and macroscopic images for 4 K mm^{-1} gradient (left on the top), SEM cross-section images of samples (center and right, on the top). **(Rectangular geometry)** Macroscopic image of 3D printed sample with inner rectangular geometry for 2 K mm^{-1} gradient (left on the bottom), SEM cross-section images of samples (center and right, on the bottom), and macroscopic images for 4 K mm^{-1} gradient (left on the bottom), SEM cross-section images of samples (center and right, on the bottom). Magnification: 50X.

dimensions are in the same range of previous studies.[22,64] The results showed positive effect in terms of *E. coli* and *S. aureus* growth inhibition indicating that loaded cryostructured scaffolds have promising characteristics for infection prevention in surgery applications.

3. Conclusion and Outlook

In this study, we developed a composite 3D structure to contemporarily induce bone regeneration and release antibiotic drug to prevent infection. 3D printed CaMgP paste-based structures

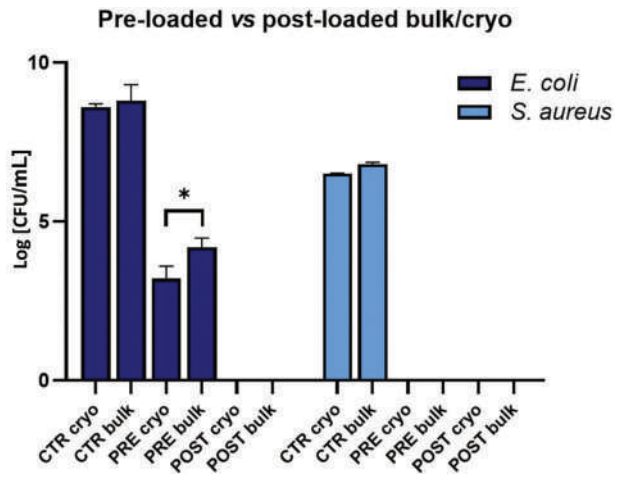

Figure 7. Inhibition of the bacterial growth (expressed as mean of log (CFU mL^{-1})) of *E. coli* and *S. aureus* strains cultivated with pre-loaded and post-loaded cryostructured and bulk samples. Two-way ANOVA with post-hoc Tukey test between experimental groups (data presented as mean ± SD, $n = 3$, * p-value ≤ 0.05).

were successfully printed with dimensions comparable to existing commercial cages for spinal fusion, and high printing accuracy (>75%) was obtained. Thus, these custom-shaped 3D constructs can potentially be combined with commercial PEEK cages and used to enhance bone tissue formation in future studies.

The hardening in DAHP solution showed the best results in terms of struvite content (≈58 wt%), and the 3D printed scaffolds revealed a compressive strength of ≈9 MPa over 28 days, comparable with that of trabecular bone. The samples survived loading for at least 5000 cycles with 300 N.

The 3D printed scaffolds were successfully combined with defined porous alginate structures obtained by cryostructuring technique and proposed for drug delivery. Due to the well-known alginate properties, the results obtained here were reproducible and they could potentially be extended to other biomedical applications. Moreover, it was observed that not only the cage and the cryostructured alginate can be combined without mismatch, but the cage shape determined the alignment and size of the cryostructured pores. This indicates that the combination of cryostructuring with 3D printed ceramics permits tailoring pore characteristics as a synergistic effect of the two methods. In addition, the porous structures were tested for their antibacterial property against *E. coli* and *S. aureus* strains, showing significant inhibition/toxicity of both pre-loaded and post-loaded drug samples, with a higher efficacy against *S. aureus*.

The material used for the system, (i.e., CaMgP and alginate) has been previously tested showing excellent biocompatibility. The CaMgP-paste based material was even evaluated in in vivo rabbit models, with no signs of adverse reactions. Hence, although an in vivo validation of the combined system will be necessary to proceed to clinical trials, we do not expect major issues in terms of compatibility. In addition, it is known that porosity and morphological cues at the microscale can even enhance cell adhesion to the implant, as well as their viability, proliferation and even differentiation, thus possibly further promoting the system biocompatibility and mitigating possible toxicity deriving from drug loading. Cell patterning/selective alignment by cryostructuring can also be foreseen as a future development, as the oriented pores could guide and tune the cell behavior. Moreover, the addition of cellular components to the system would allow to accelerate the bone healing process in spinal fusion, i.e., the final application of this research. In detail, the developed system could be employed in the lumbar spine region for the lumbar interbody fusion treatment, as the system dimensions reproduce commercial cages designed for the lumbar vertebrae. The proposed system could be easily adopted to perform the spinal fusion treatment at different spine levels (i.e., cervical, thoracic, sacral), and even extended to other applications (i.e., skeletal muscle tissue engineering, skin tissue engineering, bone tissue engineering, and drug delivery) where the control on pore orientation is beneficial. Indeed, 3D printing and cryostructuring are versatile technologies, in terms of geometry design, process, and materials selection. Therefore, the present work combining two tailorable and advanced technologies, together with the reported findings, could potentially pave the way for new therapeutic solutions, both in spinal fusion and regenerative medicine applications.

4. Experimental Section

3D Printing of Magnesium Phosphate Constructs: Inks for 3D printing were obtained starting from magnesium phosphate powders with the composition $Ca_{0.75}Mg_{2.25}(PO_4)_2$ (CaMgP), which was prepared by sintering (for 5 h at 1100 °C) a mixture of (0.5 mol) $CaHPO_4$ (Baker, Germany), (0.25 mol) $CaCO_3$ (Merck, Germany), (1.5 mol) $MgHPO_4{\cdot}3H_2O$ (Sigma–Aldrich, Germany), and (0.75 mol) $Mg(OH)_2$ (VHR Prolabo Alfa Aesar, ThermoFischer Scientific, Germany), as described before.[13] The sintered cake was manually crushed, sieved <125 µm and ground dry for 4 h at 200 rpm in a ball mill (Retsch PM400, Germany). Printable cement pastes were obtained by mixing (11 g) of CaMgP powder, (2.5 g) of magnesium oxide (MgO, Magnesia 2933), (1 g) of hydroxypropylmethylcellulose (HPMC) powder (Merck, Germany) and (10 mL) of distilled water to obtain a powder-to-liquid ratio (PLR) equal to 1.35 g mL^{-1} using a planetary vacuum mixer (Thinky, USA). After mixing, the paste was loaded in a syringe cartridge (3cc, Optimum Syringe Barrels, Nordson EFD, Germany) and aged for 24 h, prior to 3D printing.

3D models were designed by using BioCad software (RegenHU) and 3D printed at room temperature with an extrusion-based 3D printer (3D Discovery, RegenHU, Switzerland). Different geometries were printed with a pressure ranging 1.1–1.3 bar, a feedrate of 2 mm min^{-1} and a 410 µm (22 G) nozzle: filaments for fusion test in two layers based square geometry, 6 mm cylinders samples for mechanical test and more complex geometries to mimic shape and dimensions for spinal fusion. Moreover, different fiber spacings (i.e., 1, 1.5, 2 mm) and heights (i.e., 4, 7 mm) in 0–90° pattern orientation were tested. For sake of the application, the outer part of a commercial cage shape has been considered and reproduced.[37] After 3D printing, the constructs were immersed for t = 24–48 h in 3.5 M DAHP for post- hardening via the cement reaction (samples 24H DAHP, 36H DAHP, 48H DAHP). Moreover, one group of samples was sintered for 120 min at 500 °C after printing to remove the HPMC polymeric phase, followed by 24 h immersion in DAHP (SINT+24H DAHP).

The morphology of the 3D printed constructs was characterized using a stereomicroscope from the front, lateral views, and fracture surfaces obtained by cutting the scaffold in the middle with a scalpel. Fiber diameter and pores dimension were obtained from front section images and analyzed using ImageJ software. The same image has been considered for the fibers measurement; in particular $n = 11$ fibers were measured, and each fiber was measured in $n = 9$ different points. Lateral view was acquired to evaluate the adhesion between the 3D printed layers and to measure the height of the 3D printed scaffolds. Results for the performed

measurements were reported as average ± standard deviation. To evaluate printing fidelity, the so obtained dimensions ("real") were compared to the theoretical dimensions, by means of Equation (1):

$$Accuracy\,[\%] = \frac{100}{n} \times \sum_{1}^{n} \left(1 - \frac{|d_r - d_s|}{d_s}\right) \quad (1)$$

where d_r is the real sample dimension, d_s the theoretical one. This formula allows to determine whether there are significant differences between the theoretical measurements and the real ones obtained from the physical constructs. Accuracy values ≈75% are considered satisfactory.

Physical Characterization: Phase composition of printed constructs ($n = 3$) was determined by X-ray diffractometry (XRD, D5005, Siemens, Germany) using monochromatic Cu-Kα radiation. X-ray measurements were collected from $2\theta = 10$–$40°$ with a step size of 0.02° and a scan rate of 1.5 s/step. The quantitative phase composition in terms of the struvite content was quantified by means of the Rietveld method, using the software TOPAS V6 (Bruker, Germany). To determine struvite, powders from the mentioned conditions were considered and checked by the reference patterns of the ICDD database (**struvite**, PDF ref. 015–0762, **farringtonite**, PDF ref. 033–0876, **stanfieldite** PDF ref. 011–0231).

Mechanical characterization was performed in static mode on 3D printed cylinders (n = 5, Ø = 12 mm, H = 6 mm) with different fiber spacing (1, 1.5, 2 mm). Due to the limitations in extruding the CaMgP pastes by 3D printing process, a 1:2 height: diameter ratio (different from the ASTM one, being 2:1) was selected. The test was performed in uniaxial compression mode (crosshead speed = 1 mm min^{-1}) using a testing machine (Z010, Zwick/Roell, Germany) and a 10 kN load cell. 3D printed cylinders with different fiber spacing were tested after 24 h in 3.5 M DAHP. Moreover, the printed cylinders with 1 mm fiber spacing ($n = 5$ for timepoint) were mechanically tested at different timepoints (0, 1, 3, 7, 14, 21, and 28 days). Here, 3D printed samples were disinfected in ethanol for 3 h followed by immersion in phosphate buffer saline (PBS) at 37 °C, which was refreshed every two days. At each timepoint, the samples were extracted from PBS solution, triple-washed with deionized water, dried overnight (37 °C), and weighted to analyze the stability behavior. Weights at the different timepoints were expressed in terms of residual weight (RW%), and calculated by Equation (2):

$$RW\% = \frac{W_t}{W_0} X\ 100 \quad (2)$$

where W_t is the sample weight at the defined timepoint, and W_0 is the sample weight before immersion in PBS. In addition, ion release was determined by analyzing the refreshed PBS solution ($n = 5$) using inductively coupled mass spectrometry (ICP-MS, ThermoFisher Scientific, USA). Before measurements, samples were thawed and centrifuged at 14 800 rpm for 150 s. Then, 0.2 mL of the sample supernatant was diluted in 9.8 mL 0.69% HNO_3, and elemental concentrations of Mg and Ca ions were determined by comparison with standard solutions of 0.001–10 mg L^{-1}.

Afterward, the samples were again immersed in PBS for 4 h prior to mechanical testing under wet conditions. Samples surface was polished before testing. The durable cross-sectional area has been calculated by ImageJ software (1.53, National Institutes of Health). In particular, for each sample condition (i.e., 1, 1.5, and 2 mm fibers spacing), the images of the samples were loaded on ImageJ and the area of the squares pores was calculated, together with the number of pores. To calculate the durable area, the area of the circular surface area was subtracted by the number of pores multiplied by the mean of the squares surface area.

Further mechanical characterization under dynamic conditions was performed on 3D printed cylinders (n = 5, Ø = 12 mm, H = 6 mm) with 1, 1.5, and 2 mm fiber spacing. Samples were kept in wet condition (distilled water) until the beginning of the test, to mimic the physiological conditions. For testing, a universal testing machine (Z020, Zwick Roell, Germany) was used. Test was performed in cyclic mode to evaluate the sample behavior over a selected number of cycles, at room temperature. The testing protocol and related parameters according to previous studies[65,66] were adapted to the here proposed 3D printed cylinders and confirmed by a pretesting series. First, ten setting cycles were performed from 1 to 10 N rate (pre-testing region, Figure S5, Supporting Information), followed by 5000 measuring cycles from 10 to 300 N with 3 mm min^{-1} rate (cyclic loading region, Figure S5, Supporting Information). The value of force for the cyclic loading was selected according to Literature[67] and by using 30% of the maximum force (300 N, physiological load for implants) obtained in the static test for the 1 mm fiber spacing samples. After the last measuring cycle, the load was constantly increased until failure (load-to-failure region, Figure S5, Supporting Information). The parameters taken into account are i) sample integrity after 5000 measuring cycles, in accordance to previous studies on 3D scaffolds and potential bone substitutes[68–70] ii) the displacement in the cyclic loading phase, iii) the maximum load, and iv) the stiffness of the load-to-failure tests.[65,66]

Cryostructuring: An innovative in-house technology for freeze-structuring (i.e., cryostructuring) polymers and creating controlled pores by an external gradient was used. A comprehensive scheme description and functionality of the device can be found in.[30,58]

Briefly, the functioning principle was based on the solidification of solutions (i.e., hydrogel precursors) inside the cryostructuring device. The solidification occurs by using two Peltier elements arranged oppositely, which create an external temperature gradient, calculated as[27,28,30] and controlled by two programmable power supplies. Then, lyophilization process was performed to remove the ice crystals, and the structured material was crosslinked to form a stable porous structure. The distance between the Peltier elements was considered equal to 8 mm. The upper Peltier plate had a higher temperature than the lower Peltier plate, thus the heat flow was directed toward the cooler plate. Consequently, ice crystal formation occurs in antiparallel direction to the temperature gradient.

The cryostructuring process was conducted by setting a temperature of −30 °C[27] and by injecting different volumes of polymer solution depending on the used support (i.e., 3 ml in the Petri dish cover with Ø = 39 mm, H = 5 mm, 0.5-1 mL within the holes of the 3D printed construct). After cryostructuring, the samples were freeze-dried at −90 °C and P = 1 mbar (Epsilon 2–4 LSC- Christ, Germany). In this study, alginate was selected for the cryostructuring process. Indeed, it is a widely employed material in biomedical-related applications and regenerative medicine,[71,72] it is low-cost, easily retrievable, and easy to be ionic-crosslinked by calcium chloride[73] to create non-toxic and stable hydrogels. Moreover, it was previously investigated for cryostructuring.[27,74]

To cryostructure alginate, alginate solutions were prepared by magnetic stirring and degassed by centrifugation (Mega Star 1.6 R, VWR, USA) for 5 min and 4500 rpm.

First, 1 and 2% w/v alginate concentrations (JRS Pharma, Germany) were considered without the 3D printed structure, to investigate the effect of different polymer concentrations at different temperature gradients (i.e., 2, 3, and 4 K mm^{-1}) on the creation of pores with different orientation and size. Then, the influence of the 3D printed ceramic cage on the cryostructuring process (i.e., pores orientation and size) was investigated. To this aim, 3D printed scaffolds with inner circular and rectangular geometries were analyzed.

Pores microstructure evaluation was performed on freeze-dried alginate cryostructured samples by using a scanning electron microscope (Tabletop microscope TM3030 Plus, Hitachi, Japan, accelerating voltage 10 kV). Prior to image the cross section, alginate scaffolds were cut by a ceramic blade and sputter coated by a 4 nm platinum layer.

Drug Loading: Drug pre-loaded and post-loaded conditions, i.e., before and after the cryostructuring process, were investigated to evaluate the cryostructuring effect on drug efficacy. Moreover, post-loading condition is representative of the traditional antibiotic-imbibition process performed during surgical implantation.

For pre-loading condition, 6% w/v vancomycin (Merck, Germany) was mixed with 2% w/v alginate, and the solution was cryostructured (gradient 4 K mm^{-1}). Vancomycin concentration was selected based on Literature.[63,64] The cryostructured samples were crosslinked by 1 M $CaCl_2$ (Merck, Germany). Pre-loaded bulk samples were used as control.

For post-loading condition, 2% alginate was used to obtain cryostructured samples (gradient 4 K mm^{-1}), then crosslinked by $CaCl_2$. Prior to drug loading, the samples were cleaned in 5% NaOCl for 1 h, washed in milliQ water for 1 h and in 100% ethanol for 5 min. After air-drying, 6% w/v vancomycin was dissolved in milliQ water, and the samples were incubated in the drug loaded solution for 5 min. Bulk samples were used as control, to detect any difference in the release efficacy between cryostructured pores and bulk micropores.

Antibacterial Test Activity: The antibacterial activity of pre-loaded and post-loaded cryostructured samples was tested against two model pathogenic strains (1 g negative and 1 g positive), i.e., *E. coli* ATCC 8739 and *S. aureus* ATCC 6538P. All cultures were prepared by inoculating a single bacterial colony (pre-grown on Luria-Bertani (LB) agar (1.5% agar w/v) plates for 18–20 h) in 50-mL tubes with 5 mL of LB liquid medium. Cultures were grown overnight at 37 °C under agitation and then diluted to reach a final concentration of ≈10^6 CFU (Colony Forming Units) mL^{-1}. For the test, the control (samples without vancomycin loading), pre-loaded, and post-loaded bulk and cryostructured samples were placed at the bottom of 48-wells microplates that were filled with 400 µL bacterial suspensions to be further incubated for 8 h at 37 °C under shaking conditions (130 rpm). Serial dilutions of the bacterial suspensions were performed and spread onto LB agar plates to assess the bacterial growth by counting the number of CFU mL^{-1} after 24 h of growth at 37 °C in a static incubator. Triplicates were performed for each experimental condition.

Statistical Analysis: Results are expressed as mean ± standard deviation (SD) calculated from at least $n = 3$ replicates. Statistical analysis was performed using GraphPad Prism (8.0.1, GraphPad Software). Data were evaluated using two-way analysis of variance (ANOVA), followed by post-hoc Tukey correction for multiple comparison tests. The following significances were considered: * p-value ≤ 0.05, ** p-value ≤ 0.01, *** p-value ≤ 0.001, **** p-value < 0.0001.

Supporting Information

Supporting Information is available from the Wiley Online Library or from the author.

Acknowledgements

U.G. and T.J. share correspondence. The technical assistance of Michael Bartolf-Kopp for photography and the support of Isabell Biermann for fabricating the cement powders are appreciated. The authors highly appreciate support from the European Union via the EFRE Fund (European Fund for Regional Development – EFRE Bayern, Bio3D-Druck project 20-3400-2-10). T.J. would also like to thank the European Union for funding the European Union's Horizon 2020 research and innovation program under grant agreement 874827. The DFG supported the project with a "State Major Instrumentation Programme" funding for the SEM Zeiss Crossbeam 340 (INST 105022/58-1 FUGG) that enabled analysis of the samples. The authors appreciate the "Marco Polo mobility grant" support from the Department of Biomedical and Neuromotor Sciences, University of Bologna.

Open access funding enabled and organized by Projekt DEAL.

Conflict of Interest

The authors declare no conflict of interest.

Data Availability Statement

The data that support the findings of this study are available from the corresponding author upon reasonable request.

Keywords

antibacterial efficacy, custom-made prostheses, ice-templating, magnesium phosphates, orthopaedics, porous structures

Received: August 4, 2023
Revised: December 6, 2023
Published online: January 8, 2024

[1] L. Li, Z. Ling, C. Vater, X. Chen, S. Huang, Q. Qi, Z. Zhou, X. Li, Z. Zou, M. Gelinsky, J. Lou, X. Zou, M. Stiehler, *Smart Mater. Med.* **2021**, *2*, 322.
[2] M. Mokawem, G. Katzouraki, C. L. Harman, R. Lee, *J. Clin. Neurosci.* **2019**, *68*, 134.
[3] R. Yao, H. Zhou, T. J. Choma, B. K. Kwon, J. Street, *Glob. Spine J.* **2018**, *8*, 5S.
[4] B. Frost, S. Camarero-Espinosa, E. Foster, *Materials* **2019**, *12*, 253.
[5] Y. Li, Z. G. Wu, X. K. Li, Z. Guo, S. H. Wu, Y. Q. Zhang, L. Shi, S. H. Teoh, Y. C. Liu, Z. Y. Zhang, *Biomaterials* **2014**, *35*, 5647.
[6] M. Hallman, J. A. Driscoll, R. Lubbe, S. Jeong, K. Chang, M. Haleem, A. Jakus, R. Pahapill, C. Yun, R. Shah, W. K. Hsu, S. R. Stock, E. L. Hsu, *Tissue Eng. – Part A* **2021**, *27*, 26.
[7] H. N. Chia, B. M. Wu, *J. Biol. Eng.* **2015**, *9*, 4.
[8] M. Laubach, P. Kobbe, D. W. Hutmacher, *Biomaterials* **2022**, *288*, 121699.
[9] A.-V. Do, B. Khorsand, S. M. Geary, A. K. Salem, *Adv. Healthcare Mater.* **2015**, *4*, 1742.
[10] S. Chen, Y. Meng, G. Wu, Z. Liu, X. Lian, J. Hu, D. Yang, G. Zhang, K. Li, H. Zhang, *Front. Mater.* **2021**, *8*, 719536.
[11] A. R. Knutsen, S. L. Borkowski, E. Ebramzadeh, C. L. Flanagan, S. J. Hollister, S. N. Sangiorgio, *J. Mech. Behav. Biomed. Mater.* **2015**, *49*, 332.
[12] J. A. Driscoll, R. Lubbe, A. E. Jakus, K. Chang, M. Haleem, C. Yun, G. Singh, A. D. Schneider, K. M. Katchko, C. Soriano, M. Newton, T. Maerz, X. Li, K. Baker, W. K. Hsu, R. N. Shah, S. R. Stock, E. L. Hsu, *Tissue Eng. – Part A* **2020**, *26*, 157.
[13] L.-M. Götz, K. Holeczek, J. Groll, T. Jüngst, U. Gbureck, *Materials* **2021**, *14*, 5197.
[14] A. Ewald, D. Kreczy, T. Brückner, U. Gbureck, M. Bengel, A. Hoess, B. Nies, J. Bator, U. Klammert, A. Fuchs, *Materials* **2019**, *12*, 2119.
[15] B. Kanter, A. Vikman, T. Brückner, M. Schamel, U. Gbureck, A. Ignatius, *Acta Biomater.* **2018**, *69*, 352.
[16] E. Vorndran, A. Ewald, F. A. Müller, K. Zorn, A. Kufner, U. Gbureck, *J. Mater. Sci. Mater. Med.* **2011**, *22*, 429.
[17] K. Kowalewicz, E. Vorndran, F. Feichtner, A.-C. Waselau, M. Brueckner, A. Meyer-Lindenberg, *Materials* **2021**, *14*, 946.
[18] A. S. Hoffman, *Adv. Drug Delivery Rev.* **2012**, *64*, 18.
[19] A. R. Akkineni, J. Spangenberg, M. Geissler, S. Reichelt, H. Buechner, A. Lode, M. Gelinsky, *Pharmaceutics* **2021**, *13*, 1251.
[20] A. K. Gaharwar, N. A. Peppas, A. Khademhosseini, *Biotechnol. Bioeng.* **2014**, *111*, 441.
[21] Q. Chai, Y. Jiao, X. Yu, *Gels* **2017**, *3*, 6.
[22] K. Qin, R. F. P. Pereira, T. Coradin, V. De Zea Bermudez, F. M. Fernandes, *ACS Appl. Bio Mater.* **2022**, *5*, 2556.
[23] E. S. Dragan, M. V. Dinu, *React. Funct. Polym.* **2020**, *146*, 104372.
[24] M. V. Dinu, M. Pradný, E. S. Dragan, J. Michálek, *Carbohydr. Polym.* **2013**, *94*, 170.
[25] K. J. De France, F. Xu, T. Hoare, *Adv. Healthcare Mater.* **2018**, *7*, 1700927.
[26] H. Bai, A. Polini, B. Delattre, A. P. Tomsia, *Chem. Mater.* **2013**, *25*, 4551.
[27] A. Seifert, J. Gruber, U. Gbureck, J. Groll, *Adv. Eng. Mater.* **2022**, *24*, 2100860.
[28] K. Stuckensen, J. M. Lamo-Espinosa, E. Muiños-López, P. Ripalda-Cemboráin, T. López-Martínez, E. Iglesias, G. Abizanda, I. Andreu, M. Flandes-Iparraguirre, J. Pons-Villanueva, R. Elizalde, J. Nickel, A.

Ewald, U. Gbureck, F. Prósper, J. Groll, F. Granero-Moltó, *Materials* **2019**, *12*, 3105.
[29] H. Joukhdar, A. Seifert, T. Jüngst, J. Groll, M. S. Lord, J. Rnjak-Kovacina, *Adv. Mater.* **2021**, *33*, 2100091.
[30] J. G. K. Stuckensen, U. Gbureck, J. Groll, EP2788171A2, **2021**.
[31] C. K. Sun, C. J. Ke, Y. W. Lin, F. H. Lin, T. H. Tsai, J. S. Sun, *Polymers* **2021**, *13*, 414.
[32] D. Liu, Z. Liu, J. Zou, L. Li, X. Sui, B. Wang, N. Yang, B. Wang, *Front. Mater.* **2021**, *8*, 648980.
[33] H. Motasadizadeh, M. Tavakoli, S. Damoogh, F. Mottaghitalab, M. Gholami, F. Atyabi, M. Farokhi, R. Dinarvand, *Biomater. Adv.* **2022**, *139*, 213032.
[34] S. Bertlein, D. Hikimoto, G. Hochleitner, J. Hümmer, T. Jungst, M. Matsusaki, M. Akashi, J. Groll, *Small* **2018**, *14*, 1701521.
[35] G. Größbacher, M. Bartolf-Kopp, C. Gergely, P. N. Bernal, S. Florczak, M. de Ruijter, N. G. Rodriguez, J. Groll, J. Malda, T. Jungst, R. Levato, *Adv. Mater.* **2023**, *35*, 2370230.
[36] P. D. Dalton, T. B. F. Woodfield, V. Mironov, J. Groll, *Adv. Sci.* **2020**, *7*, 1902953.
[37] BASE Interfixated Titanium Surgical Technical Guide, NuVasive Inc. **2019**.
[38] J. Will, R. Melcher, C. Treul, N. Travitzky, U. Kneser, E. Polykandriotis, R. Horch, P. Greil, *J. Mater. Sci. Mater. Med.* **2008**, *19*, 2781.
[39] S. Bose, S. Vahabzadeh, A. Bandyopadhyay, *Biochem. Pharmacol.* **2013**, *16*, 496.
[40] U. K. Roopavath, S. Malferrari, A. Van Haver, F. Verstreken, S. N. Rath, D. M. Kalaskar, *Mater. Des.* **2019**, *162*, 263.
[41] L. C. Hwa, S. Rajoo, A. M. Noor, N. Ahmad, M. B. Uday, *Curr. Opin. Solid State Mater. Sci.* **2017**, *21*, 323.
[42] E. Vorndran, C. Moseke, U. Gbureck, *MRS Bull.* **2015**, *40*, 127.
[43] M. Castilho, C. Moseke, A. Ewald, U. Gbureck, J. Groll, I. Pires, J. Teßmar, E. Vorndran, *Biofabrication* **2014**, *6*, 015006.
[44] R. Gelli, L. Mati, F. Ridi, P. Baglioni, *Mater. Sci. Eng. C* **2019**, *95*, 248.
[45] F. P. W. Melchels, K. Bertoldi, R. Gabbrielli, A. H. Velders, J. Feijen, D. W. Grijpma, *Biomaterials* **2010**, *31*, 6909.
[46] A. Vedadghavami, F. Minooei, M. H. Mohammadi, S. Khetani, A. Rezaei Kolahchi, S. Mashayekhan, A. Sanati-Nezhad, *Acta Biomater.* **2017**, *62*, 42.
[47] R. J. Mondschein, A. Kanitkar, C. B. Williams, S. S. Verbridge, T. E. Long, *Biomaterials* **2017**, *140*, 170.
[48] C. Y. Lin, N. Kikuchi, S. J. Hollister, *J. Biomech.* **2004**, *37*, 623.
[49] L. Gerhardt, A. R. Boccaccini, *Materials* **2010**, *3*, 3867.
[50] M. Ginebra, E. B. Montufar, in *Bone repair biomaterials*, Woodhead Publishing, Amsterdam, Netherlands, **2019**, Ch. 9.
[51] F. Wu, J. Wei, H. Guo, F. Chen, H. Hong, C. Liu, *Acta Biomater.* **2008**, *4*, 1873.
[52] J. Jia, H. Zhou, J. Wei, X. Jiang, H. Hua, F. Chen, S. Wei, J.-W. Shin, C. Liu, *J. R. Soc. Interface* **2010**, *7*, 1171.
[53] J. Wei, J. Jia, F. Wu, S. Wei, H. Zhou, H. Zhang, J.-W. Shin, C. Liu, *Biomaterials* **2010**, *31*, 1260.
[54] C. Großardt, A. Ewald, L. M. Grover, J. E. Barralet, U. Gbureck, *TISSUE Eng. Part A* **2010**, *16*, 3687.
[55] F. Kaiser, L. Schröter, P. Wohlfahrt, I. Geroneit, J. Murek, P. Stahlhut, J. Weichhold, A. Ignatius, U. Gbureck, *J. Biomater. Appl.* **2023**, *38*, 438.
[56] F. Kaiser, L. Schröter, S. Stein, B. Krüger, J. Weichhold, P. Stahlhut, A. Ignatius, U. Gbureck, *Acta Biomater.* **2022**, *145*, 358.
[57] C. Hu, T. Ahmad, M. S. Haider, L. Hahn, P. Stahlhut, J. Groll, R. Luxenhofer, *Biofabrication* **2022**, *14*, 025005.
[58] K. Stuckensen, A. Schwab, M. Knauer, E. Muiños-López, F. Ehlicke, J. Reboredo, F. Granero-Moltó, U. Gbureck, F. Prósper, H. Walles, J. Groll, *Adv. Mater.* **2018**, *30*, 1706754.
[59] C. M. Murphy, M. G. Haugh, F. J. O'brien, *Biomaterials* **2010**, *31*, 461.
[60] H. Lin, L. Ou, Y. Lin, M. Ling, **2010**, *118*, 1878.
[61] M. Naeimi, R. Tajedin, F. Farahmandfar, M. Naeimi, M. Monajjemi, *Mater. Res. Express* **2020**, *7*, 095401.
[62] F. Wang, H. Zhou, O. P. Olademehin, S. J. Kim, P. Tao, *ACS Omega* **2018**, *3*, 37.
[63] A. Zhou, T. M. Kang, J. Yuan, C. Beppler, C. Nguyen, Z. Mao, M. Q. Nguyen, P. Yeh, J. H. Miller, *Antimicrob. Agents Chemother.* **2015**, *59*, 276.
[64] S. Ulag, A. Sahin, M. M. Guncu, B. Aksu, N. Ekren, M. Sengor, D. M. Kalaskar, O. Gunduz, *Bioprinting* **2021**, *24*, e00173.
[65] T. Brueckner, P. Heilig, M. C. Jordan, M. M. Paul, T. Blunk, R. Heribert, U. Gbureck, S. Hoelscher-doht, *Materials* **2019**, *12*, 1364.
[66] P. Heilig, P. Sandner, M. C. Jordan, R. G. Jakubietz, R. H. Meffert, U. Gbureck, S. Hoelscher-doht, *Materials* **2021**, *14*, 1925.
[67] M. Müller, V. Sleger, V. Kolar, M. Hromasová, D. Pis, R. K. Mishra, *Polymers* **2022**, *14*, 1301.
[68] F. S. Senatov, K. V. Niaza, A. A. Stepashkin, S. D. Kaloshkin, *Compos. Part B* **2016**, *97*, 193.
[69] L. Wang, Y. Qiu, H. Lv, Y. Si, L. Liu, Q. Zhang, J. Cao, *Adv. Funct. Mater.* **2019**, *29*, 1901407.
[70] R. M. S. Hoelscher-Doht, M. Jordan, C. Bonhoff, S. Frey, T. Blunk, *J. Orthop. Sci.* **2014**, *19*, 978.
[71] J. Huang, H. Fu, Z. Wang, Q. Meng, S. Liu, H. Wang, X. Zheng, J. Dai, Z. Zhang, *RSC Adv.* **2016**, *6*, 108423.
[72] M. Costantini, J. Idaszek, K. Szöke, J. Jaroszewicz, M. Dentini, A. Barbetta, J. E. Brinchmann, W. Swieszkowski, *Biofabrication* **2016**, *8*, 035002.
[73] J. Idaszek, M. Volpi, A. Paradiso, M. Nguyen Quoc, Z. Górecka, M. Klak, G. Tymicki, A. Berman, M. Wierzbicki, S. Jaworski, M. Costantini, A. Kepczynska, E. S. Chwalibóg, M. Wszola, W. Swieszkowski, *Bioprinting* **2021**, *24*, e00163.
[74] O. I. Vernaya, A. N. Ryabev, T. I. Shabatina, D. L. Karlova, A. V. Shabatin, L. N. Bulatnikova, A. M. Semenov, M. Y. Melnikov, V. I. Lozinsky, *Polymers* **2022**, *14*, 3271.